Journal of Power Sources 248 (2014) 163–171

Contents lists available at ScienceDirect

Journal of Power Sources

journal homepage: www.elsevier.com/locate/jpowsour

Properties of A-site nonstoichiometry $(Pr_{0.4})_xSr_{0.6}Co_{0.2}Fe_{0.7}Nb_{0.1}O_{3-\sigma}$ $(0.9 \leq x \leq 1.1)$ as symmetrical electrode material for solid oxide fuel cells

Peng Zhang [a], Guoqing Guan [a,b,*], Deni S. Khaerudini [a], Xiaogang Hao [c], Minfang Han [d], Yutaka Kasai [e], Kazuhiko Sasagawa [a], Abuliti Abudula [a,b,*]

[a] Graduate School of Science and Technology, Hirosaki University, 1-bunkyocho, Hirosaki 036-8560, Japan
[b] North Japan Research Institute for Sustainable Energy (NJRISE), Hirosaki University, 2-1-3 Matsubara, Aomori 030-0813, Japan
[c] Department of Chemical Engineering, Taiyuan University of Technology, Taiyuan 030024, PR China
[d] Union Research Center of Fuel Cell, School of Chemical & Environmental Engineering, China University of Mining & Technology, Beijing 100083, PR China
[e] Industrial Research Institute, Aomori Prefectural Industrial Technology Research Center, 4-11-6, Second Tonyamachi, Aomori 030-0113, Japan

HIGHLIGHTS

- P_xSCFN is synthesized as symmetrical electrode material for SOFC.
- A more fine-grained material is obtained by A-site excess of P_xSCFN.
- $P_{1.05}$SCFN shows the lowest polarization resistance both in O_2 and in wet H_2.
- As-prepared $P_{1.05}$SCFN/LSGM/$P_{1.05}$SCFN cell shows excellent performance.

GRAPHICAL ABSTRACT

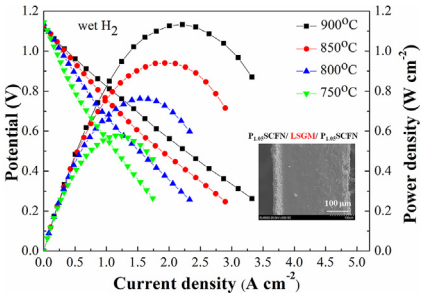

ARTICLE INFO

Article history:
Received 13 August 2013
Received in revised form
15 September 2013
Accepted 18 September 2013
Available online 27 September 2013

Keywords:
Solid-oxide fuel cells
P_xSCFN
A-site deficiency
A-site excess
Symmetrical electrode

ABSTRACT

In order to solve the carbon deposition and sulfur adsorption problems during operations of solid-oxide fuel cells (SOFCs), $(Pr_{0.4})_xSr_{0.6}Co_{0.2}Fe_{0.7}Nb_{0.1}O_{3-\sigma}$ (P_xSCFN, x = 0.9, 0.95, 1.0, 1.05 and 1.1) oxides are synthesized by the solid state reaction method and investigated as both cathode and anode for SOFCs. For P_xSCFN (x = 0.9–1.05) powders, it is found that cubic perovskite phase is formed after sintering at 1050 °C; however, when x increases to 1.1, a single impurity phase is detected for $P_{1.1}$SCFN sample by X-ray diffraction. The effects of A-site nonstoichiometry on thermal expansion coefficient, electrical conductivity and polarization resistance are investigated. The excess of A-site Pr elements in P_xSCFN (x = 1.05 and 1.1) results in a decrease in grain size and the creation of more active sites for oxygen reduction reaction. AC impedance reveals that $P_{1.05}$SCFN as symmetrical electrodes has the best electrochemical catalytic performance both in O_2 and in wet H_2 atmosphere. The maximum power densities of a $P_{1.05}$SCFN/LSGM/$P_{1.05}$SCFN cell reach as high as 1.13 W cm^{-2} in wet H_2 and 0.67 W cm^{-2} in wet CH_4 at 900 °C. Therefore, $P_{1.05}$SCFN is a potential symmetrical electrode material for SOFCs.

1. Introduction

A solid oxide fuel cell (SOFC) is an energy conversion device that produces electricity with very high efficiency by electrochemically combining a fuel and an oxidant across an ionic conducting oxide

* Corresponding authors. North Japan Research Institute for Sustainable Energy (NJRISE), Hirosaki University, 2-1-3 Matsubara, Aomori 030-0813, Japan. Tel.: +81 17 762 7756; fax: +81 17 735 5411.
E-mail addresses: guan@cc.hirosaki-u.ac.jp (G. Guan), abuliti@cc.hirosaki-u.ac.jp (A. Abudula).

0378-7753/$ – see front matter © 2013 Elsevier B.V. All rights reserved.
http://dx.doi.org/10.1016/j.jpowsour.2013.09.077

electrolyte [1]. In a standard SOFC, the cathode and anode are separated by a gastight electrolyte, such as Yttria stabilized Zirconia (YSZ), Gadolinium doped Ceria (GDC) and Strontium- and Magnesium-doped Lanthanum Gallium oxide (LSGM). The conventional anode material for SOFC is Ni–YSZ, which has a high catalytic activity for fuel oxidation, a good conductivity for current collection, low cost and a good compatibility with YSZ electrolyte. However, Ni is easily deactivated by the carbon and/or sulfur, when hydrocarbon fuels are used [2–5]. Carbon deposition and sulfur adsorption can degrade the anode performance. Internal reforming of hydrocarbon fuels often accompanies carbon deposition. The active sites of the anode will be covered with deposited carbon, leading to deactivation of the anode, loss of cell performance and lower SOFC reliability. As for the sulfur, even at concentration levels of parts per million (ppm), sulfur will be adsorbed strongly on the Ni surface and thus block its active sites for oxidation of the fuel, resulting in considerably increased anodic polarization and energy loss. In order to overcome these problems, two significant methods are considered in recent studies, one is to introduce a catalytic layer (e.g. Ru–CeO_2 [6,7]) on the fuel side of a conventional anode that acts as an internal reformer of the fuel to produce pure H_2 before it reaches the NiO/electrolyte composite; the other is to use a new anode material, such as $La_{0.75}Sr_{0.25}Cr_{0.5}Mn_{0.5}O_{3-\sigma}$ [8,9], $Sr_2Mg_{1-x}Mn_xMoO_{6-\sigma}$ [10], $BaZr_{0.1}Ce_{0.7}Y_{0.1}Yb_{0.1}O_{3-\sigma}$ [4] and $Sr_2Fe_{1.5}Mo_{0.5}O_{6-\sigma}$ [11]. Although both approaches are promising, the catalytic activity is still much lower than conventional Ni-based anode. Recently, Yang et al. [12] have reported a good redox-reversible anode material $Pr_{0.8}Sr_{1.2}(Co,Fe)_{0.8}Nb_{0.2}O_{4+\delta}$–CFA (K-PSCFN), which is obtained by annealing $Pr_{0.4}Sr_{0.6}Co_{0.2}Fe_{0.7}Nb_{0.1}O_{3-\sigma}$ (PSCFN) in H_2 at 900 °C and it shows a high catalytic activity and good stability in H_2 containing 50 ppm H_2S. However the performance of PSCFN as the cathode of SOFC is rarely reported. The cathode is usually only exposed to an oxidizing atmosphere in theory. However, when it is operated at a low cell voltage, oxygen partial pressure at the triple phase boundary (TPB) of the cathode is rather low [13]. The commonly used cathodes such as $La_{0.8}Sr_{0.2}MnO_{3-\sigma}$ (LSM) [14], $La_{0.4}Sr_{0.6}Co_{0.8}Fe_{0.2}O_{3-\sigma}$ (LSCF) [15,16] and $Ba_{0.5}Sr_{0.5}Co_{0.8}Fe_{0.2}O_{3-\sigma}$ (BSCF) [17] are not stable in a strongly reducing atmosphere, which may cause redox degradation of the cathode and thus decrease the cell performance in a long term stability test. Lots of approaches have been considered to overcome the degradation caused by cathode [15,18], and if a redox stable cathode can be used, it should be a better choice for traditional SOFC since leakage might occur when fuel is introduced into the cathode side.

$Pr_{1-x}Sr_xCo_yFe_{1-y}O_3$ (PSCF) is one of the novel cathode materials that have caught lots of attention in recent years [19–24]. Ishihara et al. found that [25] Pr-doped perovskite had the highest electrical conductivity and the lowest overpotential values owing to Pr^{3+}/Pr^{4+} valence change. PSCF with the composition, $Pr_{0.3}Sr_{0.7}Co_{0.3}Fe_{0.7}O_{3-\sigma}$ has shown polarization resistance of 0.11 Ω cm^{-2} at 700 °C in air [21]. PSCFN can be identified as having Niobium (Nb) doped into PSCF and here, Nb is for improvement of the stability of perovskites structural materials. Nagai et al. [26] reported that in $SrCoO_{3-x}$-based oxides, such as $Sr(Co_{0.9}X_{0.1})O_{3-\sigma}$ (where X = Ni, Cu, Zn, Cr, Fe, Al, Ga, In, Ce, Ti, Zr, Sn, V and Nb), $SrCo_{0.9}Nb_{0.1}O_{3-\sigma}$ has the best perovskite stability and the highest oxygen permeation. A. Radojkovic et al. [27] reported that chemical stability was enhanced with increasing Nb concentration in $BaCe_{0.9-x}Nb_xY_{0.1}O_{3-\sigma}$ structure. Elisabetta Di Bartolomeo et al. [28] also reported that $BaCe_{0.78}Nb_{0.12}Y_{0.1}O_{3-\sigma}$ had higher stability than $BaCe_{0.9}Y_{0.1}O_{3-\sigma}$. Therefore, the anode material based on PSCFN is expected to have a good performance when applied as the cathode.

Some studies have demonstrated that introducing A-site cation nonstoichiometry into the lattice structure of perovskite oxides can significantly alter the physical and chemical properties of such materials [20,22,29–34]. Li et al. [34,35] found that the ionic conductivity of A-site-deficient $(La_{0.3}Sr_{0.7})_{0.93}TiO_{3-\sigma}$ is over twice that of $La_{0.3}Sr_{0.7}TiO_{3-\sigma}$, and the chemical stability can also be improved by the introduction of A-site deficiency. Hansen [20] found that by introducing A-site deficiency into $(Pr_{0.6}Sr_{0.4})_{0.99}Co_{0.2}Fe_{0.8}O_{3-\sigma}$, the polarization resistance (R_p) decreased to 0.017 Ω cm^{-2} at 800 °C, and such materials showed lower polarization resistance than those without A-site deficiency. Zhou et al. [31,36] reported that A-site cation with both deficiency and excess of $(Ba_{0.5}Sr_{0.5})_{1\pm x}Co_{0.8}Fe_{0.2}O_{3-\sigma}$, or $(BS)_{1\pm x}CF$, oxides created additional oxygen vacancies. Especially for appropriate A-site excess of $(BS)_{1+0.3}CF$, the oxygen adsorption process was promoted.

In this study, PSCFN is used as both the anode and cathode materials. The process for the preparation of the cells will become simpler, where the electrodes may be fired using the same thermal process. This would significantly reduce cost, and be an important concept for practical application. The effect of A-site cation non-stoichiometry on the performance of P_xSCFN ($0.9 \le x \le 1.1$) oxides is evaluated in details. Particularly, the effects of A-site deficiency/excess on electrical conductivity, sinterability and thermal expansion coefficient, impedance spectroscopy and the performances of symmetrical cells of P_xSCFN/LSGM/P_xSCFN are investigated. A possible charge compensation mechanism associated with A-site nonstoichiometry is proposed.

2. Experimental

2.1. Sample preparation and cell fabrication

A-site nonstoichiometry $(Pr_{0.4})_xSr_{0.6}Co_{0.2}Fe_{0.7}Nb_{0.1}O_{3-\sigma}$ (P_xSCFN) (x = 0.9, 0.95, 1.0, 1.05 and 1.1) perovskite oxides were prepared by solid-state reaction from the materials with high purity: $Pr(NO_3)_3\cdot 6H_2O$, $SrCO_3$, $Co(NO_3)_2\cdot 6H_2O$, Fe_2O_3 and Nb_2O_5 (99.9% Wako, Japan). These materials were mixed by ball milling. The calcinations of the precursor powders were performed at 1050 °C for 5 h in air to obtain a pure phase. Then, such oxides were ball milled again for 12 h. After that, the finely ground oxide powders were pressed into bars ($30 \times 5 \times 3$ mm^3) under a uniaxial pressure of 200 MPa. The bar samples obtained were further sintered at 1200 °C for 5 h in air at a heating rate of 3 °C min^{-1} before undergoing a conductivity test. The densities were determined by Archimedes method and only those samples with relative densities higher than 90% were used for characterizations. The commercially available powder, $La_{0.8}Sr_{0.2}Ga_{0.8}Mg_{0.2}O_{3-\sigma}$ (LSGM, 99.9% FCM, USA) was used for preparation of the electrolyte. Dense LSGM pellets with 20 mm diameter were prepared by uniaxial mold pressing the LSGM powders at 200 MPa and then sintering at 1450 °C for 10 h in air. The thickness of the LSGM electrolyte was controlled to 800 μm for the impedance test but to 265 μm for the cell performance test.

Symmetrical cells of P_xSCFN/LSGM/P_xSCFN for impedance studies were prepared by a slurry coating method. That is, P_xSCFN slurry was coated onto both sides of the LSGM electrolyte pellet (with a thickness of 265 μm) to form the anode and cathode and then, the as-prepared cell was sintered in air at 1200 °C for 2 h. For a single cell performance testing, the cell was sealed on an alumina tube using a Pyrex glass ring, which was found to seal the cell very well.

2.2. Material characterization

Crystallographic phases of the P_xSCFN powders were carried out using X-ray diffraction (XRD, Shimadazu, XD-610, Japan) with Cu-Kα radiation. The morphology and element composition were investigated by scanning electron microscopy (SEM, Hitachi,

SU6600, Japan) with an Energy Dispersive X-ray Detector (EDX). The electrical conductivity was measured by four-terminal DC method on sintered P_xSCFN bars in different gas atmospheres at ascending temperature ranging from 200 to 900 °C, with an interval of 50 °C and a dwell of 10 min at each temperature before the conductivities were measured to allow the system to equilibrate. The thermal expansion coefficient (TEC) of the samples was measured between 30 and 900 °C using a dilatometer (TA Instruments, Q400), with a heating rate of 2 °C min^{-1}.

Electrochemical measurements were performed in half-cell and symmetrical cell for polarization resistance and cell performance test, respectively. These measurements were carried out in the temperature range of 750–900 °C. Electrochemical impedance spectra (EIS) of the half-cell were recorded at open circuit voltage (OCV) over the frequency range of 0.01 Hz–1 MHz with the AC signal amplitude of 10 mV using a frequency response analyzer and a potentiostat (Solartron 1255B and 1287, respectively). The impedance responses were analyzed using the equivalent RC circuit method. For the single cell performance test, the anode was first annealed at 900 °C in 5% H_2 atmosphere with balance of Ar for 1 h, and then exposed to fuel at a flow rate of 100 cm^3 min^{-1}. O_2 was used on the cathode side as the oxidant with a flow rate of 50 cm^3 min^{-1}. Electronic contacts were realized by using a Pt mesh with Pt paste. Based on previous work [3,37–39], the Pt should have almost no influence on the electrode catalytic activity. The impedance of the single cell after the cell performance test was measured at OCV using the same method.

3. Results and discussion

3.1. Phase and microstructure characteristics

Fig. 1 shows XRD patterns of the synthesized P_xSCFN ($x = 0.9$–1.1) powders sintered at 1050 °C for 5 h. The peaks for all the samples of $x \leq 1.05$ matched a cubic perovskite phase. The absence of other peaks indicated that any additional phases were present below the detection limit and that the different A-site deficiency material obtained was therefore of high phase-purity. However, for the sample with $x = 1.1$, an impurity phase was observed at $2\theta = 31.7°$. Therefore, the excess limit of Pr element in P_xSCFN at 1050 °C in air should be approximately 5 mol%.

Typical SEM images of the surface and cross section of the sintered P_xSCFN bars are shown in Fig. 2(a)–(e) and (f)–(j), respectively. Sometimes, even small variations in the composition of perovskite

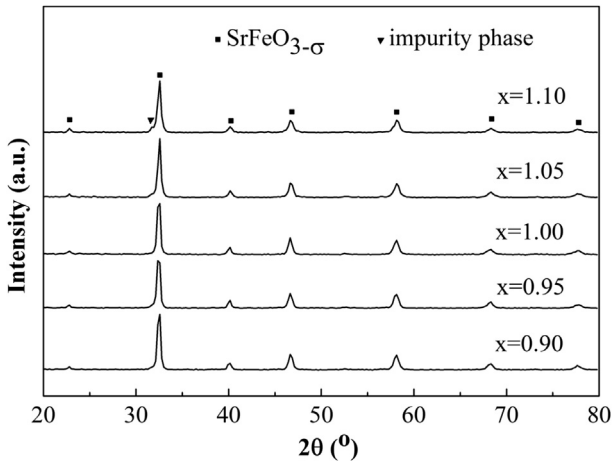

Fig. 1. X-ray diffraction patterns of P_xSCFN ($x = 0.9$–1.1) sintered in air at 1050 °C for 5 h.

oxides could change both physical and chemical properties significantly. As shown in Fig. 2(a)–(e), grain boundaries were obviously observed between the grains on the surface of the P_xSCFN ($x = 0.9$–1.1) for all samples. The grain diameters were approximately 4 and 2 μm in the cases of $x \leq 1.0$ and $x > 1.0$, respectively. With the increase in the content of Pr, the grain size decreased. More triple-phase boundary (TPB), which acts as an important influence in the performance of the cell, could be provided due to the smaller grain size. Similar phenomenon was also reported by Jaffe et al. [40] and Zhou et al. [31]. On the other hand, as shown in Fig. 2(f)–(j), P_xSCFN samples with $x = 0.9$, 0.95 and 1.0 were much denser than those with $x = 1.05$ and 1.1, suggesting that the A-site deficiency promoted the sinterability of PSCFN materials. Similar phenomenon was also observed in other works [41–43]. Li et al. [41] found that the A-site deficiency of $(La_{0.3}Sr_{0.7})_{0.95}Sc_{0.10}Ti_{0.90}O_{3-\delta}$ enhanced sinterability by promoting the diffusion of A-site big ions. Roosmalen et al. [42] thought that the introduction of A-site deficiency into (La,Sr)MnO_3 could facilitate the diffusion rate of A-site cations and thus in turn enhance the sintering process. Ge et al. [43] believed that A-site deficiency could improve the rate of cation bulk diffusion and as a result, the densification process was enhanced. However, in this study, it should be noted that for the samples of $x = 1.05$ and 1.1, no interconnected holes were observed, indicating that both samples had good density. Based on Archimedes method, it is found that their relative densities were higher than 90%.

3.2. Electrical conductivity performance

Temperature dependence of electrical conductivity of PSCFN in different gas atmosphere is shown in Fig. 3. One can see that the electrical conductivity increased with the increase in oxidant partial pressure. This followed small polaron semiconducting behavior, in which the electron holes serve as the charge carriers. In this case, the electronic conductivity is usually at least two orders of magnitude higher than the ionic conductivity, and as such, the measured electrical conductivity can be regarded as the electronic conductivity [44–46]. As shown in Fig. 3, the conductivity had the highest values for temperatures up to 450–500 °C, and then decreased with further increase in temperature. The decrease in electrical conductivity over this temperature may be caused by the loss of lattice oxygen [47]. The loss of lattice oxygen of the perovskite materials could generate oxygen vacancies, and results in the decrease in the concentration of charge or the annihilation of electron holes, as described in Eq. (1):

$$O_O^{\times} + 2h^{\bullet} = V_O^{\bullet\bullet} + \frac{1}{2}O_2(g) \quad (1)$$

where $O_O^{\times}$ is the lattice oxygen, $h^{\bullet}$ is the electrons hole and $V_O^{\bullet\bullet}$ is the oxygen vacancy. Thus, the electronic conductivity should decrease. Herein, the value of electrical conductivity of PSCFN reached as high as 107 S cm^{-1} in air at 900 °C, which met the requirement of an SOFC cathode.

Fig. 4 shows the influence of different Pr contents in electrical conductivity of P_xSCFN. One can see that all samples displayed a similar trend: the electrical conductivity first increased and then decreased by further increasing the temperature to over 500 °C. By increasing A-site deficiency (decreasing x value from 1.0 to 0.9), the conductivity decreased. Based on the defect chemistry and electroneutrality principle, the valence of A-site decreased by increasing A-site deficiency, but it can be compensated by increasing B-site valence or increasing oxygen vacancy concentration. As presented in Eq. (1), oxygen vacancy generation can release the electronic and annihilation of electron holes, resulting in the decrease in electrical conductivity. Co and Fe elements on B-site

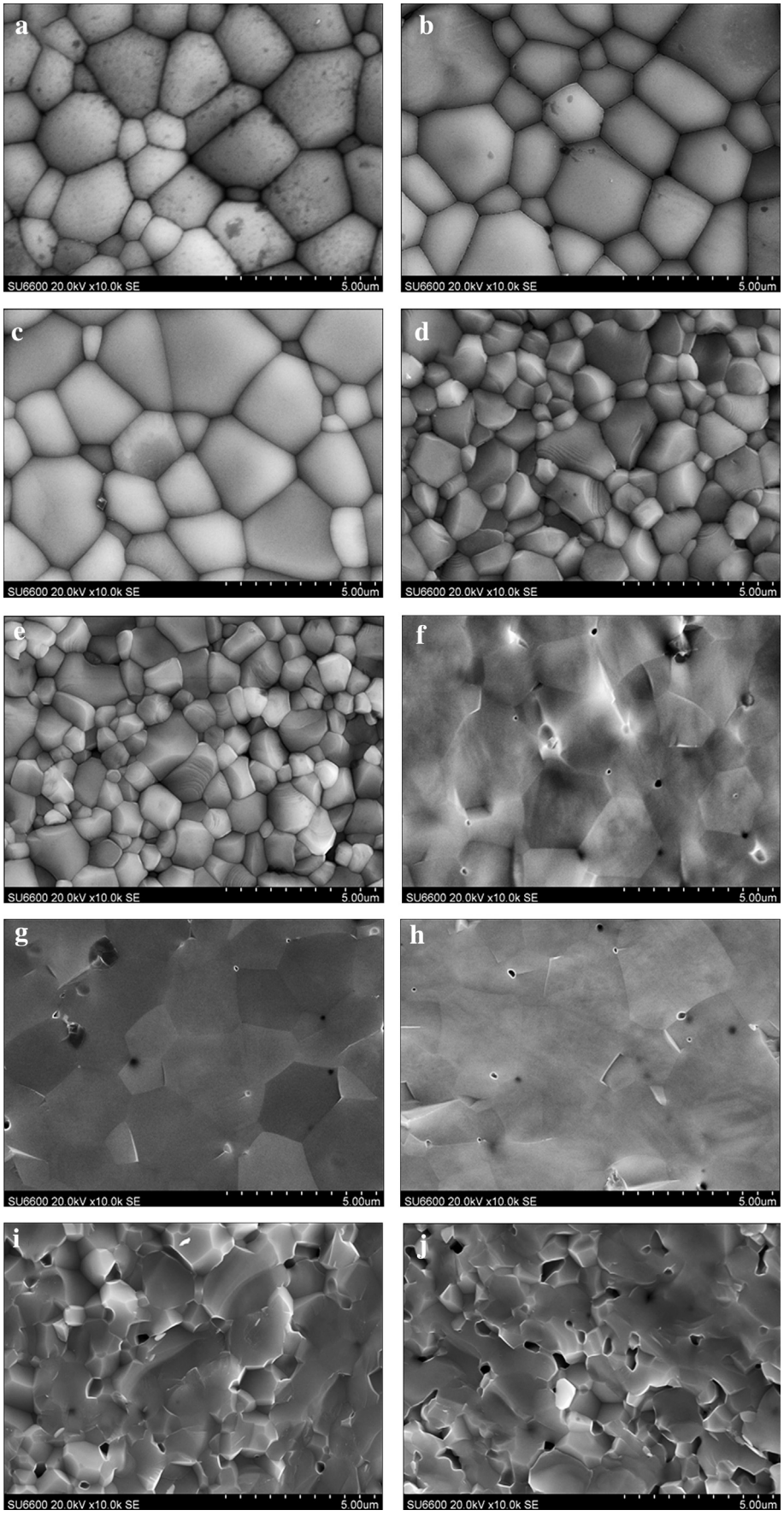

Fig. 2. Typical SEM images of P_xSCFN after sintered at 1200 °C for 5 h: (a–e) surface of $x = 0.9$, 0.95, 1.0, 1.05 and 1.1, respectively; and (f–j) cross section of $x = 0.9$, 0.95, 1.0, 1.05 and 1.1, respectively.

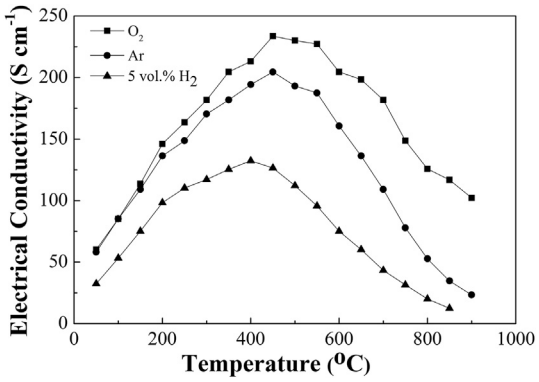

Fig. 3. Temperature dependence of electrical conductivity of PSCFN in different gas atmosphere.

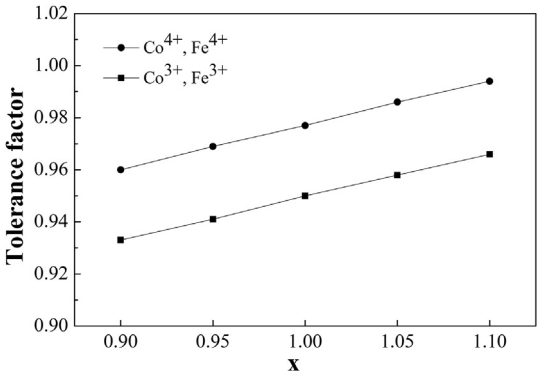

Fig. 5. Tolerance factor of $(Pr_{0.4})_xSr_{0.6}Co_{0.2}Fe_{0.7}Nb_{0.1}O_{3-\sigma}$ ($x = 0.9$–1.1).

should have valence alternations between Co^{3+} and Co^{4+} and/or between Fe^{3+} and Fe^{4+}, which coexist in B-site. B-site ions in low valence state could lead to decrease in $Co^{\$}_{Co}$(hole) and $Fe^{\$}_{Fe}$(hole) concentrations and consequently decrease in hole conductivity [36]. When x value increased from 1.0 to 1.05, i.e., to an A-site excess state, the valence compensation should be achieved by decreasing B-site valence state. For materials with perfect cubic perovskite structure (ABO_3), the ionic radii of all the elements must obey Eq. (2):

$$(r_A + r_O) = \sqrt{2}(r_B + r_O) \tag{2}$$

where r_A, r_B and r_O are the effective ionic radii of the A-site, B-site and oxygen, respectively. The Goldschmidt tolerance factor t can be used to measure the structural stability, which is calculated according to Eq. (3):

$$t = \frac{r_A + r_O}{\sqrt{2}(r_B + r_O)} \tag{3}$$

In general, the ideal value of t is 1, and the cubic perovskite structure can be maintained when $0.88 \leq t \leq 1.09$ [22,23]. The stability of the structure requires the t value to be near 1. Fig. 5 presents the tolerance factor for t which is dependent on the x value for P_xSCFN. One can see that all t values were less than 1. In particular, by increasing A-site deficiency, the value of t deviated significantly from 1. In order to maintain the structural stability of the P_xSCFN cubic perovskite, the t value should be larger (near 1) during the structure formation process. Therefore, the radii of B-site are required to be as small as possible, with a larger number of B-site ions in a higher valence state. Herein, it should be noted that Co^{4+} (0.053 nm) and Fe^{4+} (0.0585 nm) are smaller than Co^{3+} (0.0545 nm) and Fe^{3+} (0.0645 nm), and thus, more Co^{4+} and Fe^{4+} ions are required. From the above analysis, decrease of Co^{4+} and Fe^{4+} concentrations could lead to decrease in electronic holes of Co and Fe concentrations and consequently decrease of the electronic conductivity and perovskite structural stability. In other words, increasing oxygen vacancy concentrations can lead to decrease in electronic conductivity. It indicates that the compensation is mainly caused by increasing the oxygen vacancy concentration with the increase of A-site deficiency in the case that x value is less than 1.0. However, in this case, it could result in the decrease in Co^{4+} and Fe^{4+} concentrations and the increase in oxygen vacancy concentration by A-site excess, as observed by Zhou et al. [36].

3.3. Thermal expansion behavior and chemical compatibility

Fig. 6 shows the thermal expansion curves for different A-site components. The average TEC of the P_xSCFN ($x = 0.95$, 1.0 and 1.05) in the range of 20–900 °C were ca. 18.41×10^{-6}, 18.70×10^{-6} and 18.02×10^{-6} K^{-1} for $x = 0.95$, 1.0 and 1.05, respectively. Obviously, the average TEC of the P_xSCFN electrode sample was lower than the reported value for $Pr_{1-x}Sr_xCo_{0.8}Fe_{0.2}O_{3-\sigma}$ (19.7–21.23×10^{-6} K^{-1}) [19], and similar to that for $(Pr_{0.6}Sr_{0.4})_{0.99}Co_{0.2}Fe_{0.8}O_{3-\sigma}$ (18.67×10^{-6} K^{-1}) [20,29]. It is possibly caused by the lower Co contents in P_xSCFN, owing to the smaller ionic radius of iron compared with that of cobalt [48]. As shown in Fig. 6, all of the curves were nonlinear and the value of L/L_0 increased upon heating at the beginning stage, and then began to experience an inflection range occurring at temperatures between 550 and 750 °C. It should be mainly attributed to the loss of lattice oxygen and the formation of oxygen vacancies [49].

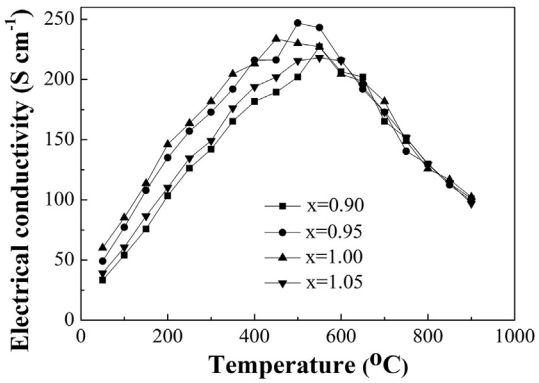

Fig. 4. Temperature dependence of electrical conductivity of P_xSCFN ($x = 0.9$, 0.95, 1.0, 1.05 and 1.1) in air.

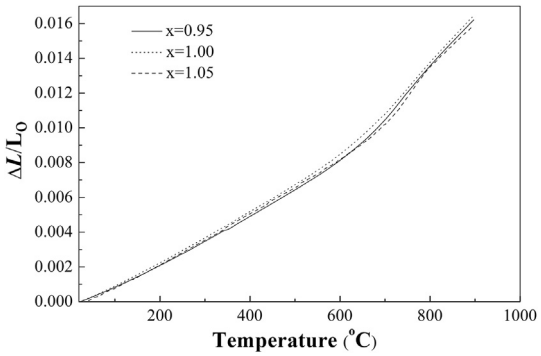

Fig. 6. Thermal expansion curves for $(Pr_{0.4})_xSr_{0.6}Co_{0.2}Fe_{0.7}Nb_{0.1}O_{3-\delta}$ ($x = 0.95$, 1.0 and 1.05) as a function of temperature.

Chemical compatibilities of P_xSCFN and LSGM electrolyte were also evaluated. The P_xSCFN and LSGM powders were ball-milled in ethanol for 6 h with a weight ratio of 1:1, and then sintered at 1200 °C for 10 h, and the XRD patterns are shown in Fig. 7. One can see that there was no additional phase formation within the detectable limit of XRD for all Pr contents, indicating that there was no interface reaction taking place between the LSGM electrolyte and PSCFN electrode when sintered at 1200 °C for 10 h.

3.4. Impedance analysis

Fig. 8 shows typical impedance plots from the symmetric electrode measurements in O_2 at different temperatures. Since the value of polarization resistance is highly related to the microstructure and thickness of the electrode, all the samples were prepared at the same conditions, i.e., the same ratio of powder and pore former, the same calcination temperature and the same duration for slurry coating. In order to compare the value of polarization resistance, ohmic resistance was set as zero. The impedances were measured under OCV condition. As shown in Fig. 8, the polarization resistance decreased with an increase in Pr element content from $x = 0.9$–1.05, but when x was further increased to 1.1, the polarization resistance also increased, i.e., the resistances were 0.020, 0.018, 0.016, 0.012, and 0.022 Ω cm^{-2} at 850 °C for $x = 0.9$, 0.95, 1.0, 1.05 and 1.1, respectively. The measured impedance spectra can be divided into three parts by frequency region: high frequency region (HFR, ~10^4 Hz), medium frequency region (MFR, ~10^2 Hz) and low frequency region (LFR, ~10^{-1} Hz). The HFR is usually related to the grain boundary of the electrolyte [50], which will not be discussed here. The arc of MFR may be caused by the dissociation of oxygen into the oxide ion as well as the charge transfer at the interface, and it should be related to the kinetics of the reactions determined by the electrochemical activity of the electrode materials, the electrical conductivity of the electrode current collector and the ionic conductivity between the electrode and electrolyte. The LFR is presumably associated with the non-charge transfer processes, such as gas-phase diffusion, oxygen surface exchange at TPB, and oxygen ion diffusion in the bulk of the electrode [21,51–53].

Fig. 9 shows the impedance curves with frequency for P_xSCFN ($x = 0.95$–1.1) electrode measured at 850 °C and under open circuit condition. One can see that the main polarization resistance of P_xSCFN in O_2 was produced in the medium frequency region (MFR), indicating that it was caused by the electrochemical activity of the electrode materials. Furthermore, the cathode performances were enhanced by increasing the amount of Pr concentration ($x = 0.95$–1.05) and the polarization resistance of sample $P_{1.05}$SCFN reached the lowest value, suggesting that the highest catalytic activity of oxygen reduction was achieved at this concentration. However, when x was further increased to 1.1, the polarization resistance

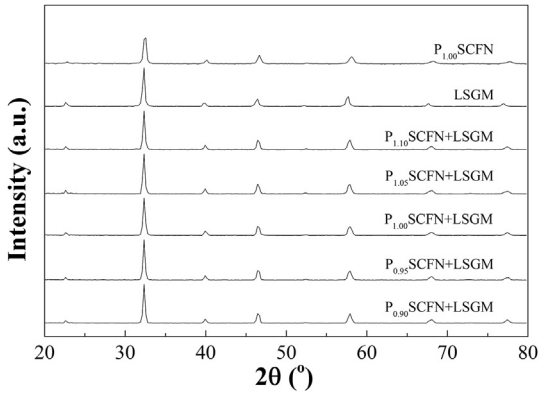

Fig. 7. X-ray diffraction patterns of perovskite $(Pr_{0.4})_xSr_{0.6}Co_{0.2}Fe_{0.7}Nb_{0.1}O_{3-\delta}$ powder, pure $La_{0.8}Sr_{0.2}Ga_{0.8}Mg_{0.2}O_{3-\delta}$ (LSGM) powder, and PSCFN + LSGM mixture sintered in air at 1200 °C for 5 h.

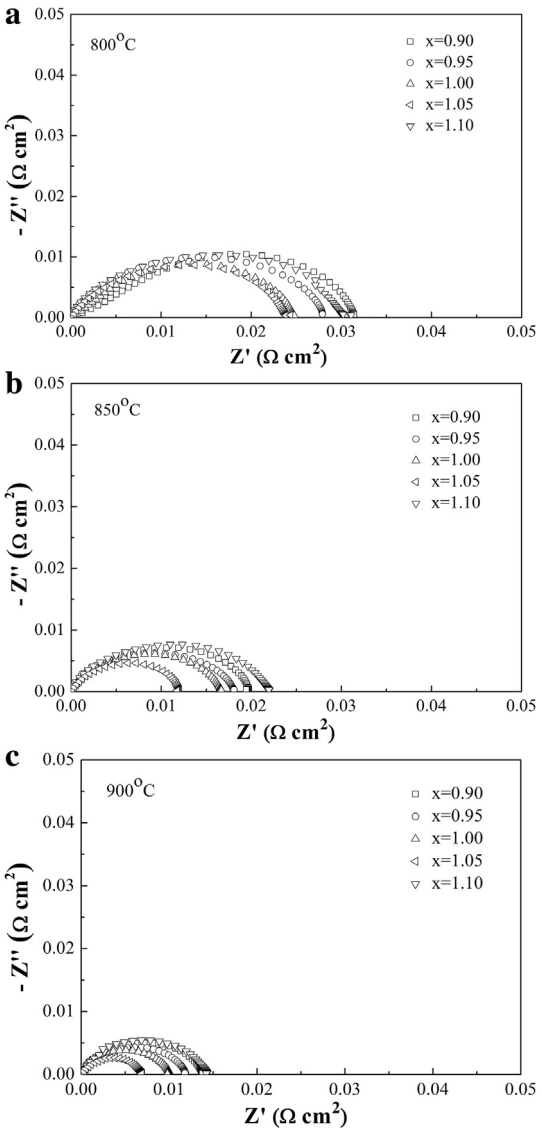

Fig. 8. Impedance spectroscopy for PSCFN symmetrical half cells using LSGM as electrolyte and PSCFN as electrode tested in O_2 at various temperatures.

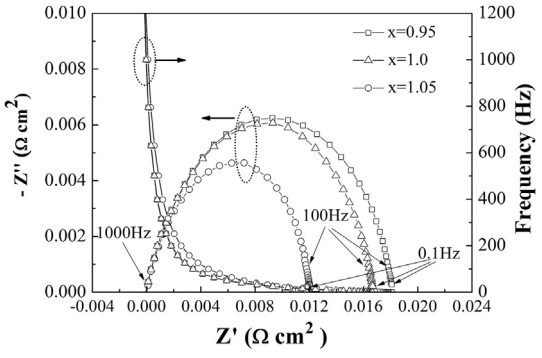

Fig. 9. Impedance curves with frequency for P_xSCFN electrode measured at 850 °C and open circuit.

increased and in this case, it is found that an impurity phase was formed (as indicated in Fig. 1), such impurities could have negative effect on the cathode performance. Praseodymium could change its oxidation state, i.e., change between Pr^{3+}/Pr^{4+} [20,54], and thus, it should have some catalytic activity towards the reduction of oxygen. On the other hand, such change between Pr^{3+}/Pr^{4+} could be promoted by increasing the Pr concentration, resulting in the enhancement of the catalytic activity in the reduction of oxygen. This phenomenon was also found in other systems [20]. In addition, as stated in Section 3.1, the grain size of $P_{1.05}$SCFN was smaller than that of other P_xSCFN ($x = 0.9$, 0.95 and 1.0) and thus, it could provide more triple-phase boundary for redox reaction, influencing the performance of the cell.

Fig. 10 shows impedance spectra of PSCFN tested in humidified H_2 (3% H_2O). In order to show the polarization resistance clearly, the bulk resistance for each sample was normalized to zero. One can see that all of the diagrams consisted of two semicircles originated from the interface processes associated to the electrical capacitive. To separate these two processes, the impedance spectra were fitted via an equivalent circuit with a configuration of L R_{ohm} (R_{HF} − CPE$_{HF}$)(R_{LF} − CPE$_{LF}$). Here, R_{ohm} is the overall/total ohmic resistance including the electrolyte resistance, electrode ohmic resistance and lead resistance; L is the inductance, which could be dependent on the Pt current/voltage probes or the high-frequency phase shift of the electrochemical equipment; CPE$_{HF}$ and R_{HF} are presumably related to the double layer capacitance and charge transfer impedance at the interface between the electrolyte and electrode; CPE$_{LF}$ and R_{LF} probably relate to the electrochemical kinetics of the electrode material such as adsorption and/or diffusion processes of the reactant and/or product to/from the interface. Similar models were also used in the literature for comparable systems [3,36,52]. The electrode polarization resistance $R_p = R_{HF} + R_{LF}$, can be obtained from the intercepts on the real axes of the impedance plot. As shown in Fig. 10, the polarization resistance decreased apparently with increasing A-site Pr contents when that x value was less than 1.05. With further increase in x to 1.1, the polarization resistance also increased. The fitted impedance results for PSCFN are given in Table 1, in which the effect of A-site Pr element contents on the total electrode polarization resistance (R_p) as well as the high- and low-frequencies (R_{HF} and R_{LF}) at 850 °C was indicated. The R_{HF} decreased by increasing A-site Pr content while the R_{LF} remained constant as x increased from 0.9 to 1.05, indicating that the charge transfer impedance at the interface between the

Table 1
Fitted impedance results of P_xSCFN ($x = 0.9$, 0.95, 1.0, 1.05 and 1.1) as symmetric electrode in wet H_2 at 850 °C.

Sample	R_p (Ω cm^{-2})	R_{HF} (Ω cm^{-2})	R_{LF} (Ω cm^{-2})
$P_{0.90}$SCFN	0.38	0.27	0.11
$P_{0.95}$ScFN	0.27	0.19	0.08
$P_{1.00}$SCFN	0.22	0.14	0.08
$P_{1.05}$ScFN	0.15	0.07	0.08
$P_{1.10}$SCFN	0.26	0.18	0.08

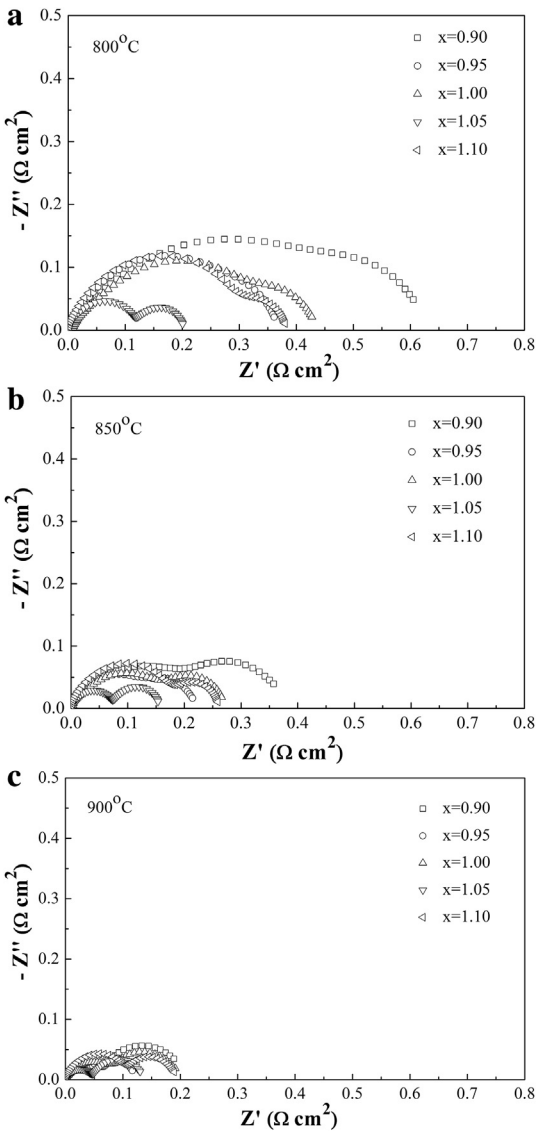

Fig. 10. Impedance spectroscopy of PSCFN symmetrical half cells using LSGM as electrolyte in wet H_2 at various temperatures.

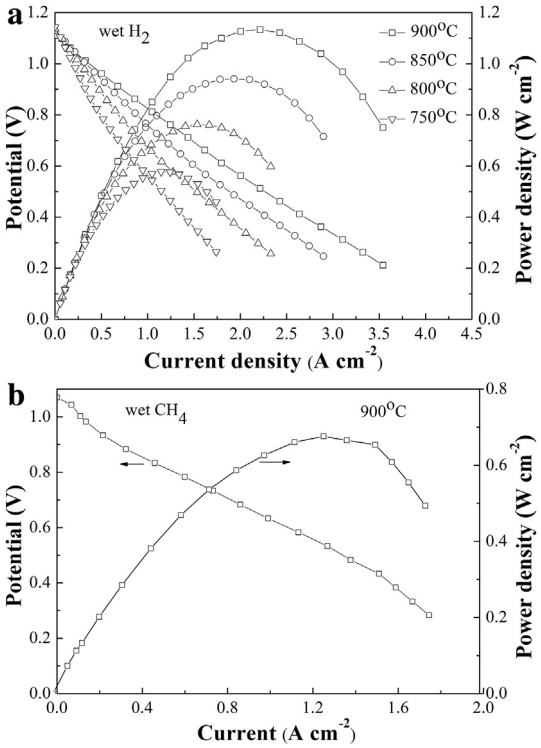

Fig. 11. I–V and I–P curves of the single cells with the $P_{1.05}$SCFN as the both anode and cathode with LSGM electrolyte supported: a) in wet H_2 and b) in wet CH_4.

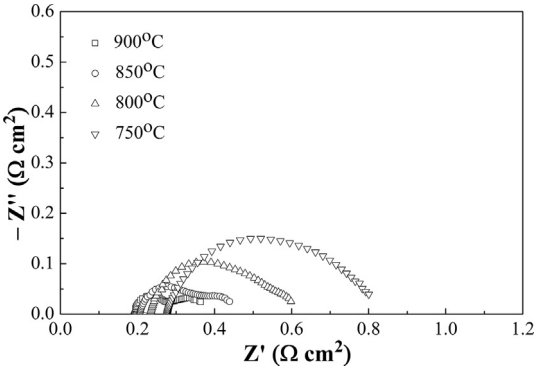

Fig. 12. Impedance spectra for the single cell with $P_{1.05}$SCFN as the symmetrical electrode measured under OCV using wet H_2 as fuel and O_2 as oxidant at different temperatures.

electrolyte and the electrode decreased with increasing Pr content. However, the bulk diffusion resistance obtained from all these P_xSCFN electrodes showed a similar value. It should be noted that $P_{1.05}$SCFN electrode exhibited ultra low polarization resistances, with values of 0.20, 0.15 and 0.135 Ω cm^{-2} at 800, 850 and 900 °C, respectively, indicating that $P_{1.05}$SCFN had high activity for electrochemical oxidation of H_2 at such temperatures. Therefore, in this study, $P_{1.05}$SCFN was selected to fabricate symmetric SOFC, in which $P_{1.05}$SCFN served as both anode and cathode on LSGM electrolyte.

3.5. Cell performance

The performance of as-fabricated LSGM electrolyte supported $P_{1.05}$SCFN/LSGM/$P_{1.05}$SCFN single cell was investigated using wet H_2 or wet CH_4 with 3 mol% water as fuel and pure O_2 as oxidant gas on the cathode side. The thickness of the LSGM electrolyte was ca. 265 μm. At 900 °C, the open circuit voltages (OCV) were 1.12 V when using wet H_2 and 1.07 when using wet CH_4 as fuel, respectively. Fig. 11(a) shows *I–V* as well as *I–P* curves of the cell operated at 750–900 °C in wet H_2. The maximum power densities of 1.13 and 0.94 W cm^{-2} were achieved at the temperatures of 900 and 850 °C, respectively. Fig. 11(b) shows *I–V* as well as *I–P* curves of the cell operated in CH_4 at 900 °C. In this case, the maximum power density was 0.67 W cm^{-2}. Fig. 12 shows the typical impedance spectra of this symmetric cell under open-circuit condition with wet H_2 as fuel at different temperatures. Here, the intercept on the real axis at high frequencies represents the ohmic resistance (R_{ohm}) from the electrolyte, the electrodes, the connection wires and the testing conditions [55]. The lowest frequency intercept on the real axis represents the total resistance of the cell. The distance between the two intercepts corresponds to the interfacial resistance (R_p), which mainly corresponds to the adsorption and diffusion process of oxygen on the cathode and hydrogen on the anode. Based on the results in Fig. 12, the R_{ohm} of the single cell were 0.28, 0.23, 0.21 and 0.19 Ω cm^{-2} at 750, 800, 850 and 900 °C, respectively while the R_p were 0.26 and 0.20 Ω cm^{-2} at 850 and 900 °C, respectively.

Fig. 13 shows the interfaces of $P_{1.05}$SCFN/LSGM/$P_{1.05}$SCFN for the cell after testing in wet H_2 and CH_4 at 750–900 °C. One can see that the thicknesses of the $P_{1.05}$SCFN, LSGM and $P_{1.05}$SCFN were ca. 25, 265 and 25 μm, respectively. Fig. 13(b) and (c) revealed that the $P_{1.05}$SCFN electrode and LSGM electrolyte matched very well. Fig. 13(d) indicated that the surface of the anode material had a homogeneous pore distribution with grain sizes ranging from 1 to 2 μm.

4. Conclusions

A potential material P_xSCFN ($0.9 \leq x \leq 1.1$) which can be used as both anode and cathode for SOFC is synthesized by solid state reaction method and characterized. It is found that cubic perovskite phase is formed after sintering at 1050 °C in air when *x* is in the range of 0.9–1.05. However, an impurity phase is formed if *x* is over 1.1. All prepared P_xSCFN samples show good chemical compatibility

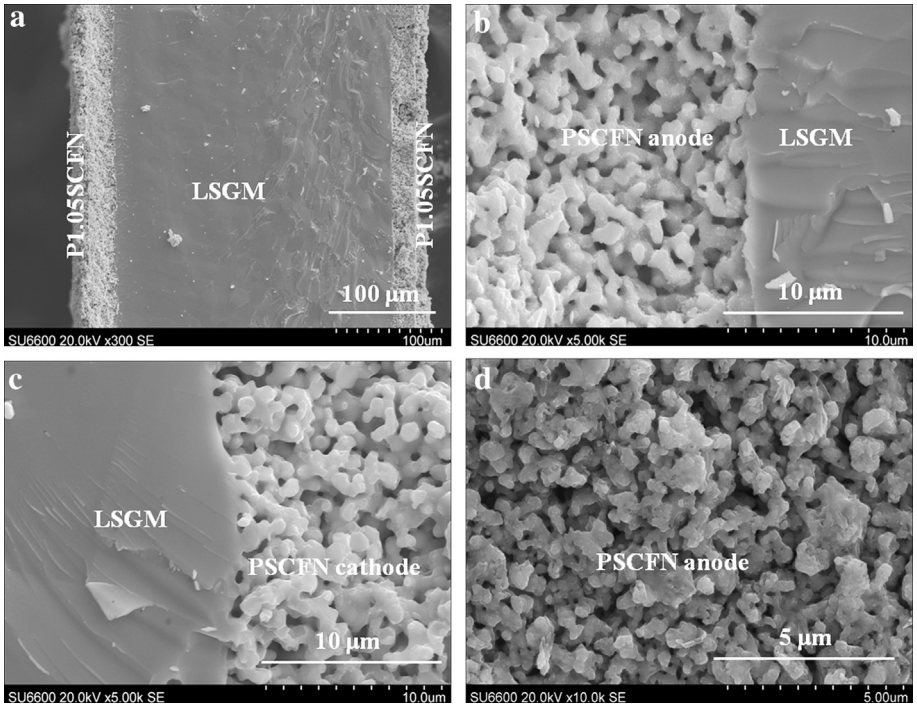

Fig. 13. Typical SEM images for the cell after testing in wet H_2 and wet CH_4 at 750–900 °C: (a) cross section of the cell configuration, (b) cross section between $P_{1.05}$SCFN anode and LSGM; (c) cross section between LSGM and $P_{1.05}$SCFN cathode; (d) surface of the $P_{1.05}$SCFN anode.

with LSGM electrolyte after sintering at 1200 °C for 10 h. In the cases of A-site Pr element excess, i.e., $P_{1.05}$SCFN and $P_{1.1}$SCFN, a more fine-grained material is obtained. The conductivity is found to be increased by increasing A-site Pr content with P_xSCFN in which $x = 0.9–1.0$. However, the electronic conductivity decreases by further increasing Pr content. In particular, $P_{1.05}$SCFN shows the lowest polarization resistance both in O_2 and in wet H_2, with the values of 0.012 and 0.15 Ω cm^{-2} at 850 °C, respectively. The maximum power densities of the fabricated symmetric SOFC cell of $P_{1.05}$SCFN/LSGM/$P_{1.05}$SCFN reach 1.13 and 0.67 W cm^{-2} at 900 °C with wet H_2 and CH_4 as fuels, respectively, indicating that $P_{1.05}$SCFN should be a potential candidate as a novel symmetric electrode material for SOFCs.

Acknowledgments

This study was supported by Aomori City Government. P. Zhang gratefully acknowledges the scholarship from the State Scholarship Fund of China Scholarship Council (2012) and Deni S. Khaerudini gratefully acknowledges the scholarship from the Ministry of Education, Culture, Sports, Science and Technology (MEXT) of Japan. The authors also thank Professor Takeshi Kubota at NJRISE and Dr Seiji Kakuta at Aomori Prefectural Industrial Technology Research Center for their technical support on experiments.

References

[1] H.Y. Tu, Y. Takeda, N. Imanishi, O. Yamamoto, Solid State Ionics 117 (1999) 277–281.
[2] M. Gong, X. Liu, J. Trembly, C. Johnson, J. Power Sources 168 (2007) 289–298.
[3] H. Lv, H. Tu, B. Zhao, Y. Wu, K. Hu, Solid State Ionics 177 (2007) 3467–3472.
[4] L. Yang, S. Wang, K. Blinn, M. Liu, Z. Liu, Z. Cheng, M. Liu, Science 326 (2009) 126–129.
[5] S.W. Tao, J.T.S. Irvine, Adv. Mater. 18 (2006) 1581–1584.
[6] C. Sun, Z. Xie, C. Xia, H. Li, L. Chen, Electrochem. Commun. 8 (2006) 833–838.
[7] Z. Zhan, S.A. Barnett, Science 308 (2005) 844–847.
[8] T. Wenyi, Z. Qin, Y. Han, Z. Xiufang, L. Hongyi, Int. J. Hydrogen Energy 37 (2012) 7398–7404.
[9] S. Tao, J.T. Irvine, Nat. Mater. 2 (2003) 320–323.
[10] Y.H. Huang, R.I. Dass, Z.L. Xing, J.B. Goodenough, Science 312 (2006) 254–257.
[11] Q. Liu, X. Dong, G. Xiao, F. Zhao, F. Chen, Adv. Mater. 22 (2010) 5478–5482.
[12] C. Yang, Z. Yang, C. Jin, G. Xiao, F. Chen, M. Han, Adv. Mater. 24 (2012) 1439–1443.
[13] D.M. Bastidas, S. Tao, J.T.S. Irvine, J. Mater. Chem. 16 (2006) 1603–1605.
[14] V.A.C. Haanappel, J. Mertens, D. Rutenbeck, C. Tropartz, W. Herzhof, D. Sebold, F. Tietz, J. Power Sources 141 (2005) 216–226.
[15] H.J. Hwang, J.-W. Moon, S. Lee, E.A. Lee, J. Power Sources 145 (2005) 243–248.
[16] L. Qiu, Solid State Ionics 158 (2003) 55–65.
[17] Z. Shao, S.M. Haile, J. Ahn, P.D. Ronney, Z. Zhan, S.A. Barnett, Nature 435 (2005) 795–798.
[18] K. Fujita, K. Ogasawara, Y. Matsuzaki, T. Sakurai, J. Power Sources 131 (2004) 261–269.
[19] X. Meng, S. Lü, Y. Ji, T. Wei, Y. Zhang, J. Power Sources 183 (2008) 581–585.
[20] K.K. Hansen, J. Electrochem. Soc. 156 (10) (2009) B1257–B1260.
[21] K. Park, C. Lee, J. Bae, Y. Yoo, Int. J. Hydrogen Energy 34 (2009) 6852–6860.
[22] P.K. Patro, T. Delahaye, E. Bouyer, Solid State Ionics 181 (2010) 1378–1386.
[23] Y. Guo, Y. Yin, Z. Tong, J. Yin, M. Xiong, Z. Ma, Solid State Ionics 193 (2011) 18–22.
[24] Y. Yin, M. Xiong, N. Yang, Z. Tong, Y. Guo, Z. Ma, E. Sun, J. Yamanis, B. Jing, Int. J. Hydrogen Energy 36 (2011) 3989–3996.
[25] T. Ishihara, T. Kudo, H. Matsuda, Y. Takita, J. Electrochem. Soc. 142 (5) (1995) 1519–1524.
[26] T. Nagai, W. Ito, T. Sakon, Solid State Ionics 177 (2007) 3433–3444.
[27] A. Radojkovic, M. Zunic, S.M. Savic, G. Brankovic, Z. Brankovic, Ceram. Int. 39 (2013) 307–313.
[28] E.D. Bartolomeo, A. D'Epifanio, C. Pugnalini, F. Giannici, A. Longo, A. Martorana, S. Licoccia, J. Power Sources 199 (2012) 201–206.
[29] G.C. Kostogloudis, C. Ftikos, Solid State Ionics 126 (1999) 143–151.
[30] K. Hansen, K. Hansen, Solid State Ionics 178 (2007) 1379–1384.
[31] W. Zhou, R. Ran, Z. Shao, W. Jin, N. Xu, J. Power Sources 182 (2008) 24–31.
[32] F. Tietz, V.A.C. Haanappel, A. Mai, J. Mertens, D. Stöver, J. Power Sources 156 (2006) 20–22.
[33] Z. Liu, L.-Z. Cheng, M.-F. Han, J. Power Sources 196 (2011) 868–871.
[34] P. Zhang, S. Song, M. Han, Mater. Lett. 104 (2013) 1–4.
[35] X. Li, H. Zhao, X. Zhou, N. Xu, Z. Xie, N. Chen, Int. J. Hydrogen Energy 35 (2010) 7913–7918.
[36] W. Zhou, R. Ran, Z. Shao, W. Zhuang, J. Jia, H. Gu, W. Jin, N. Xu, Acta Mater. 56 (2008) 2687–2698.
[37] S. Park, J.M. Vohs, R.J. Gorte, Nature 404 (2000) 265–267.
[38] S. Tao, J.T.S. Irvine, J. Electrochem. Soc. 151 (4) (2004) A497–A503.
[39] R. Martínez-Coronado, J.A. Alonso, A. Aguadero, M.T. Fernández-Díaz, Int. J. Hydrogen Energy (2013). http://dx.doi.org/10.1016/j.ijhydene.2013.04.149.
[40] B. Jaffe, W.R. Cook, H. Jaffe, Piezoelectric Ceramics, Academic Press, New York, 1971.
[41] X. Li, H. Zhao, D. Luo, K. Huang, Mater. Lett. 65 (2011) 2624–2627.
[42] J.A.M. Van Roosmalen, E.H.P. Cordfunke, J. Solid State Chem. 110 (1994) 106–108.
[43] L. Ge, W. Zhou, R. Ran, S. Liu, Z. Shao, W. Jin, N. Xu, J. Membr. Sci. 306 (2007) 318–328.
[44] Y. Cheng, H. Zhao, D. Teng, F. Li, X. Lu, W. Ding, J. Membr. Sci. 322 (2008) 484–490.
[45] K. Zhang, R. Ran, L. Ge, Z. Shao, W. Jin, N. Xu, J. Membr. Sci. 323 (2008) 436–443.
[46] P.J. Gellings, H.J.M. Bouwmeester, Catal. Today 58 (2000) 1–53.
[47] S. Song, P. Zhang, M. Han, S.C. Singhal, J. Membr. Sci. 415-416 (2012) 654–662.
[48] Z.-B. Yang, M.-F. Han, P. Zhu, F. Zhao, F. Chen, Int. J. Hydrogen Energy 36 (2011) 9162–9168.
[49] H. Ullmann, N. Trofimenko, F. Tietz, D. Stover, A. Ahmad-Khanlou, Solid State Ionics 138 (2000) 79–90.
[50] J. Kim, G.-D. Kim, J. Moon, Y. Park, W. Lee, K. Kobayashi, M. Nagai, C. Kim, Solid State Ionics 143 (2001) 379–389.
[51] S.B. Adler, Chem. Rev. 104 (2004) 4791–4843.
[52] F. Qiang, K. Sun, N. Zhang, X. Zhu, S. Le, D. Zhou, J. Power Sources 168 (2007) 338–345.
[53] X.J. Chen, S.H. Chan, K.A. Khor, Electrochim. Acta 49 (2004) 1851–1861.
[54] F. Jin, Y. Shen, R. Wang, T. He, J. Power Sources 234 (2013) 244–251.
[55] T. Wei, Y. Ji, X. Meng, Y. Zhang, Electrochem. Commun. 10 (2008) 1369–1372.